The interaction of crossover formation and the dynamic architecture of the synaptonemal complex during meiosis

Simone Köhler[1,2,*], Michal Wojcik[3,4,*], Ke Xu[3,4,5,6,#] and Abby F. Dernburg[1,2,5,7,#]

1. Department of Molecular and Cell Biology, University of California, Berkeley, Berkeley CA 94720-3220
2. Howard Hughes Medical Institute, 4000 Jones Bridge Road, Chevy Chase, MD 20815
3. Department of Chemistry, University of California, Berkeley, Berkeley CA 94720-3220
4. Chan Zuckerberg Biohub, San Francisco, CA 94158, USA
5. California Institute for Quantitative Biosciences, Berkeley CA 94720
6. Division of Molecular Biophysics and Integrated Bioimaging, Lawrence Berkeley National Laboratory, Berkeley, CA 94720
7. Division of Biological Systems and Engineering, Lawrence Berkeley National Laboratory, Berkeley CA 94720

* these authors contributed equally to this work.

corresponding authors:

Ke Xu <xuk@berkeley.edu>

Abby F. Dernburg < afdernburg@berkeley.edu >

During meiosis, chromosomes pair with their homologous partners, and a structure known as the synaptonemal complex (SC) assembles between them. Evidence indicates that this material plays a role in regulating crossover recombination between homologs, although this remains controversial. Here we use three-dimensional STochastic Optical Reconstruction Microscopy (3D-STORM) to interrogate the molecular architecture of the SC in intact germline tissue from *Caenorhabditis elegans*, and analyze its ultrastructure during meiotic progression. Using a probabilistic mapping approach, we determine the position and orientation of the four known SC structural proteins. We report that a marked structural transition occurs within this material upon crossover designation. We also identify a mutation that disturbs both SC ultrastructure and crossover interference, the widespread mechanism that results in non-randomly wide spacing of crossovers between the same chromosome pair. Together with other evidence, our findings suggest that the SC is an active material, and that structural transitions may directly contribute to chromosome-wide crossover regulation.

The synaptonemal complex (SC) is a protein structure that assembles between homologous chromosomes during meiotic prophase, stabilizing their parallel alignment [1]. The SC appears as a periodic ladder-like structure in electron micrographs [2]. Recent studies have revealed that this material shows dynamic, liquid-like behavior [3-7]. The SC is required for and appears to regulate meiotic recombination [3, 8-13]. Despite its central role in meiosis, the molecular organization of the SC remains poorly characterized.

In *C. elegans,* the SC assembles between homologs even in the absence of meiotic recombination [14]. Four structural proteins essential for SC assembly have been identified: SYP-1, SYP-2, SYP-3, and SYP-4 [15-18]. Limited information about their organization within the SC has been obtained through protein-protein interaction analysis and immuno-electron microscopy [19]. Super-resolution microscopy has emerged as a powerful tool to investigate the organization of macromolecular assemblies, including the SC [20, 21]. We recently described the molecular architecture of meiotic chromosome axes, which form the substrate for SC assembly, based on 3D-STORM [22, 23] in intact *C. elegans* gonads [24]. Here, we apply this approach to analyze the organization of the SC during meiotic prophase.

Results

Using antibodies that bind either short peptides within SC proteins or epitope tags inserted by genome editing, we localized the SYP proteins along paired meiotic chromosomes using 3D-STORM and averaging methods (Extended Data Fig. S1). The orientation of the SC in our images was defined by labeling a reference protein in the chromosome axes, HIM-3 [25]. For positional mapping of SC proteins, we analyzed regions that were observed in frontal view (Fig. 1b, c). We rotated all images about the optical axis (*z*-axis) such that the chromosomes are extended along the *y*-axis, with the SC spanning the distance between the homologs on the *x*-axis (Extended Data Fig. S1b-c, methods). Taking advantage of the well-characterized progression of meiotic stages within the germline of adult *C. elegans*, we compared SC organization before, during and after the designation of crossover sites (Fig. 1a).

Dynamic architecture of the synaptonemal complex in *C. elegans*

The width of the SC in *x* in *C. elegans*, as measured from electron micrographs, is approximately 96 nm [3]. An antibody recognizing the C-terminal peptide of SYP-1 was resolved as two parallel strands, located at 42.3±0.8 nm and 42.0±1.2 nm off-center in early and late pachytene, respectively (Fig. 1b, m). This epitope thus lies near the outer edges of the SC and within a few nanometers of HIM-3, the most proximal known component of the chromosome axis (Table S1)[24]. Intriguingly, in cross-sectional views (*xz*-view, Fig. 1c) we observed striking differences in its distribution in *z* between early and late pachytene SCs: While the C-terminus of SYP-1 was confined near the central plane in early pachytene, it was widely distributed in *z* in late pachytene (Fig. 1d, e, m, center and Table S1).

We then asked whether the N-terminus of SYP-1 is similarly relocalized during meiotic progression. Tagging the N-terminus of SYP-1 disrupts SC assembly ([26] and data not shown), but we identified a poorly conserved region close to the N-terminus in which insertion of an HA epitope did not impair function (Table S2). Interestingly, this epitope was confined to a thin plane in the center of the SC along both the *x* and *z* axis in both early and late pachytene SCs (Fig. 1d, e, m, top). Our data support a transverse orientation for SYP-1, as previously reported [19], with its N-terminus at the center and C-terminus near the axes. Thus, SYP-1 appears to be an ortholog of "transverse filament" proteins from other organisms [27-31]. Importantly, these localization data are inconsistent with a uniform growth in thickness of the SC through e.g.

87 lateral stacking of SYP-1 molecules during meiotic progression, which has previously been
88 suggested based on observations of increased fluorescence intensity during late pachytene in
89 budding yeast [4] and *C. elegans* [5]. The distinct localization patterns of N- and C-terminal
90 epitopes in early and late SCs along the *z* axis suggest a more complex reorganization of SYP-1
91 during meiosis.
92 To further probe the orientation of SYP-1 within the SC, we mapped the N-terminal
93 localization events to the C-terminal distributions, assuming a rigid, rod-like conformation (Fig.
94 S2a-b, see methods). Our approach indicated that SYP-1 lies nearly parallel to the SC in early
95 pachytene, but is diagonally oriented in late pachytene (Fig. 2a-b).

96 We next asked how the organization of other SC components was affected by meiotic
97 progression. We mapped the C-termini of SYP-2, SYP-3-HA and SYP-4-HA, the N-terminus of
98 GFP-SYP-3[32], and an epitope inserted into the middle of SYP-4 (Table S2, Fig. 1d, e, m and
99 Extended Data Fig. S3). The results are summarized in Table S1. We observed consistent
100 differences between early and late pachytene for most epitopes, particularly for the C-terminus of
101 SYP-4, which moves from a central plane in early pachytene to a splayed orientation, protruding
102 above and below the central plane of the SC, in late pachytene (Fig. S2c and S3, Table S1).
103 Similarly, epitopes on SYP-2 and SYP-3 were more central in early pachytene than late
104 pachytene (Fig. 1d,e,m, S2c and Fig. S3). We further found that SYP-3 localized at (N) or close
105 to (C) the midline of the SC in *x*, suggesting a head-to-head arrangement of SYP-3 molecules
106 (Fig. S3 and Table S1). These findings are inconsistent with one conclusion of a previous study,
107 that the C-terminus of SYP-3 lies in proximity to the axes [19]. This discrepancy may reflect the
108 challenges of determining the orientation of the SC in samples prepared for immuno-EM.
109 Overall, 3D-STORM imaging and probabilistic modeling provide new insights into SC
110 ultrastructure and reveal a marked reorganization of SC components during meiotic progression
111 (Fig. S2c).

112 **Crossover formation is accompanied by a change in synaptonemal complex organization**
113 Programmed double-strand breaks (DSBs) are generated during early prophase. A subset
114 eventually gives rise to crossover (CO) recombination events. In *C. elegans* each pair of
115 homologous chromosomes undergoes only a single CO, while all other breaks are repaired to
116 yield noncrossover products. Some of the key signaling molecules that regulate CO site selection

117 localize to the SC [3, 11-13, 33, 34], and the integrity of this structure is important for CO
118 regulation [9]. Previous work from our group revealed that the SC behaves as a liquid crystal[3],
119 suggesting that diffusing signals and/or structural transitions could be propagated through this
120 material [35]. Interestingly, recent evidence suggests that the central region of the SC grows in
121 length and/or thickness throughout the pachytene stage of meiotic prophase, and that SC proteins
122 may become more stably associated with this structure upon crossover formation [4-7, 9]. Thus,
123 we wondered whether the dramatic reorganization of the SC during meiotic prophase might be
124 linked to crossover formation and might provide a structural basis for the SC's role in CO
125 regulation. We therefore first asked whether the timing of SC reorganization coincides with CO
126 designation. In *C. elegans*, designated crossovers can be visualized as bright GFP-COSA-1 foci,
127 which are first detected in mid-pachytene [36] (Fig. 1a). To test whether the structural transition
128 within the SC coincides with the appearance of bright GFP-COSA-1 foci, we imaged nuclei at
129 mid-pachytene within intact gonads. We inferred the crossover designation status of individual
130 nuclei based on the detection of bright COSA-1 foci and classified them as either mid(-)
131 pachytene or mid(+) pachytene. Throughout mid-pachytene, SYP-1 retains its transverse
132 orientation and both N- and C-termini of SYP-1 are widely distributed in *z* (Fig. 1f,g,m and
133 Table S1). This is consistent with a lateral stacking of SYP-1 molecules in parallel orientation, as
134 observed in early pachytene (Fig. 2a,b). However, the distance of the C-termini of SYP-1 from
135 the central axis of the SC in frontal view was drastically lower in mid(+) pachytene nuclei
136 compared to SCs in mid(-) pachytene nuclei.
137 This indicates that the designation of COs coincides with a conformational switch within
138 the SC. To take an unbiased approach to analyze the dynamics of SC organization during meiotic
139 prophase, we employed principal component analysis (PCA) of SYP-1 and SYP-2 distributions
140 (see methods). The first dimension in the PCA, indicative of the main changes within the SC
141 across different stages during meiotic prophase, corresponds to the transition from early to late
142 pachytene SCs (Fig. 2c). Mid(+) pachytene SCs are similar to late pachytene SCs along the first
143 principal component, while mid(-) SCs are in between early and late pachytene SCs, indicating
144 that the SC is reorganized upon CO designation.
145 In *C. elegans*, designation of COs triggers the asymmetrical remodeling of chromosome
146 axes and the SC to create two domains on either side, known as the long and the short arm.
147 Downstream steps in this differentiation require the recruitment of the Polo-like kinase PLK-2 to

148 the SC [5, 37, 38]. To assess whether the changes we observe in SC ultrastructure are dependent
149 on crossover designation and/or the subsequent remodeling processes, we determined the
150 organization of the SC in *zhp-3(jf61)* null mutants, which lack crossovers [39], and in *plk-*
151 *2(ok1936)* null mutants, which are proficient for CO designation but show pronounced delays in
152 downstream remodeling and arm differentiation [5, 7, 37, 40], although they do eventually
153 segregate most chromosomes properly [38]. We found that SCs in late pachytene in *zhp-3(jf61)*
154 mutants resembled those in early pachytene nuclei in wild-type hermaphrodites, while SCs at late
155 pachytene in *plk-2(ok1936)* mutants are very similar to wild-type (Fig. 1h,i,n, 2 and Fig. S3c,e).
156 Thus, structural reorganization of the SC requires CO designation but is independent of PLK-2.
157 We note that PLK-2 also plays an early role in homologous paring and synapsis [37, 40], and our
158 super-resolution images reveal severe defects in SC architecture in *plk-2(ok1936)* null mutants
159 despite the overall similarity to wild-type late pachytene SCs (Fig. 1i, n). Similarly, while the
160 global SC architecture in *zhp-3(jf61)* mutants resembled early pachytene SCs in wild type, the
161 SC increased in thickness along the optical axis during pachytene in *zhp-3(jf61)* oocytes, based
162 on the spatial distribution of SYP-1 (Fig. 1h, n), consistent with the continuous incorporation of
163 SC subunits even in the absence of crossover formation [5]. In summary, our data indicate that
164 the SC grows in thickness from early to late pachytene independent of crossovers, while the
165 reorganization of SC ultrastructure requires and coincides with CO designation.
166
167 **Defects in SC organization are linked to defects in crossover interference**
168 The SC plays a critical role in regulating the number and distribution of CO
169 recombination events [3, 8, 9, 12, 13]. We therefore wondered whether reorganization of the SC
170 is linked to CO regulation. Fortuitously, in our efforts to isolate a functional C-terminally tagged
171 *syp-4* allele, we identified an unusual, partially functional allele, *syp-4(ie25)* (Fig. 3a). In *syp-*
172 *4(ie25)* homozygotes, we observed timely homologous synapsis, as determined by the length of
173 the transition zone, which corresponds to the leptotene and zygotene stages of meiosis. Six
174 bivalents were consistently observed at diakinesis, indicative of CO formation on all six
175 chromosome pairs (Fig. 3b, c, e). However, super-resolution microscopy indicated that the
176 architecture of the SC was drastically altered in *syp-4(ie25)* late pachytene after crossover
177 formation (Fig. 1l and 2, Extended Fig. S3). SYP-1 lies in a highly tilted orientation (Fig. 2a,b)
178 and the overall conformation of the SC in *syp-4(ie25)* at late pachytene is clearly distinct from

179 any conformation in wild-type animals in our principal component analysis (Fig. 2c). In contrast,
180 early pachytene SCs in *syp-4(ie25)* are more reminiscent of SC conformation of prior to CO
181 formation in wild-type animals (Fig. 1k and 2). These data suggest a strong defect in SC
182 organization in *syp-4(ie25)* that is exacerbated upon CO designation (Fig. 2c).
183 Notably, *syp-4(ie25)* mutant hermaphrodites exhibited high frequencies of chromosome
184 missegregation, resulting in embryonic lethality (38±4% survival, compared to 104% in wild-
185 type) and male self-progeny (6±1% compared to 0.1% in wild-type, Table S2), albeit less severe
186 than in a *syp-4(tm2713)* deletion allele (2.5% viability and 40% males) [18]. Importantly,
187 crossover formation was severely impacted in *syp-4(ie25)*: We observed a slight delay in meiotic
188 progression, indicated by a modest extension of CHK-2 kinase activity [41] (Fig. 3d) and an
189 accumulation of RAD-51 foci, which mark unrepaired recombination intermediates (Extended
190 Data Fig. S4). Moreover, the structure of bivalents at diakinesis was altered in *syp-4(ie25)*
191 oocytes (Fig. 3f), indicating that crossover formation might be affected [42, 43].
192 To better characterize the effects of *syp-4(ie25),* we imaged GFP-COSA-1 to quantify
193 designated crossover sites at late pachynema [36]. Wild-type animals display a single bright
194 GFP-COSA-1 focus on each of the 6 chromosome pairs, even when the number of DSBs is
195 markedly increased [36, 42]. In contrast to the 6±0.2 (s.d.) GFP-COSA-1 foci we observed in
196 wild-type and heterozygous *ie25/+* animals, we observed 10.9±1.7 GFP-COSA-1 foci at late
197 pachytene in homozygous *syp-4(ie25)* hermaphrodites (Fig. 3g, h). This suggested that crossover
198 interference, which in wild-type animals acts over distances longer than any single chromosome
199 [9, 42], is greatly decreased in *syp-4(ie25)* homozygotes. To test this hypothesis, we use two
200 different metrics to quantify the crossover interference strength, the gamma factor [44] and the
201 coefficient of coincidence [45]. Each of these approaches confirmed that crossover interference
202 is severely reduced or absent in *syp-4(ie25)* mutants (Fig. 3i,j).
203 To verify that GFP-COSA-1 foci indeed correspond to designated crossover sites in wild-
204 type and *syp-4(ie25)* animals, we also measured crossing-over genetically using whole genome
205 sequencing (see methods). This confirmed that crossovers in *syp-4(ie25)* homozygotes match the
206 number of GFP-COSA-1 foci. Thus, *syp-4(ie25)* mutants are proficient for synapsis, yet they
207 exhibit drastic alterations in SC architecture and cannot impose normal crossover interference.
208 Crossover interference acts along the physical length of the synapsed chromosomes, and
209 in some organisms chromosomes with longer axes undergo more crossovers than chromosomes

210 with shorter axes [46-49]. Therefore, we next asked whether the axis length is increased in *syp-*
211 *4(ie25)* mutants. Interestingly, axes in *syp-4(ie25)* mutants are shorter than in wild-type animals.
212 Thus, changes in axis length cannot account for the observed increase in COs in *syp-4(ie25)*
213 mutants. We hypothesize that the increase in CO number may be caused by the defects in SC
214 organization in *syp-4(ie25)* mutants.

215 Partial depletion of SC proteins in *C. elegans* by RNAi can result in a slight increase in
216 the number of crossovers, to about 7 GFP-COSA-1 foci per nucleus [9]. Thus, we tested whether
217 the defect in crossover regulation in *syp-4(ie25)* can be attributed to reduced levels of SC
218 proteins. The abundance of an epitope-tagged HA-SYP-1 was not altered by the *syp-4(ie25)*
219 mutation (Fig. S5a). However, the immunofluorescence signal of SYP-1 and SYP-2 was reduced
220 in *syp-4(ie25),* although staining appeared contiguous along the chromosomes (Fig. S5b, c). This
221 indicates the *syp-4(ie25)* mutation impairs assembly of SYP proteins between chromosomes. In
222 contrast, we also isolated a mutant, *syp-4(ie27)* (Fig. S6a), which reduced expression levels of
223 SYP-4-HA to about 30% of wild-type (Fig. S6c). Both the transition zone and CHK-2 active
224 zone were extended in *syp-4(ie27)* single mutants, indicating that completion of synapsis and CO
225 designation were delayed (Fig. 3c-d, Fig. S6b, d). We also observed a slight increase in the
226 number of GFP-COSA-1 foci to 7±1.1 (Fig. S6e, Fig. 3g), which is comparable to results
227 obtained for partial depletion of SYP-1, -2 or -3 by RNAi [9], but distinct from our results for
228 *syp-4(ie25)*. This indicates that the defects in crossover interference in *syp-4(ie25)* are not a mere
229 consequence of reduced protein expression.

230 To test whether the defects in SC ultrastructure can account for the effects of *syp-4(ie25)*
231 on crossover regulation, we investigated the role of *syp-4(ie25)* in the regulation of COSA-1 foci
232 within aggregates of SC proteins known as polycomplexes. These bodies self-assemble prior to
233 or after synapsis in many organisms, including in early meiotic nuclei in *C. elegans*. Large
234 polycomplexes also assemble in meiotic nuclei in worms lacking the axis protein HTP-3, and
235 show periodic striations in orthogonal directions that correspond precisely to the width and
236 longitudinal banding of the SC [3, 50]. Intriguingly, we have found that polycomplexes in *htp-3*
237 null mutants recapitulate key aspects of the spatial patterning of CO proteins normally seen along
238 SCs, although these mutant animals lack DSBs and meiotic recombination intermediates.
239 Specifically, at late pachytene, most polycomplexes display a single COSA-1 focus (1.1±0.2;
240 Fig. 4a, b) [3]. When we combined the *syp-4(ie27)* mutation, which reduces expression of SYP-

241 4, with Δ*htp-3*, this resulted in smaller polycomplexes, but they showed an identical number of
242 GFP-COSA-1 foci at late pachytene (1.1±0.2) (Fig. 4a, b). By contrast, when *syp-4(ie25)* was
243 combined with Δ*htp-3,* multiple GFP-COSA-1 foci (2.1±0.8) were associated with each
244 polycomplex (Fig. 4a, b), mirroring the ~2-fold increase in GFP-COSA-1 foci observed along
245 bona fide SCs in *syp-4(ie25)* mutants.
246 We thus interrogated the organization of polycomplexes in *syp-4(ie25)* by EM. While
247 structures resembling the electron-dark lateral and brighter, striated central regions were
248 observed in *Δhtp-3 syp-4(ie25)*, the overall organization was dramatically altered: polycomplexes
249 appeared to be internally fragmented, rather than maintaining constant orientation over hundreds
250 of nm, as in "normal" polycomplexes [3] (Fig. 4c), and the distance between parallel electron-
251 dark bands was much narrower (46.3±1.2 nm, vs 97.6±1.5 nm in *Δhtp-3* polycomplexes, Fig.
252 4c), This likely reflects differences in organization and/or orientation of SYP proteins within
253 polycomplexes. Overall, the disorganized structure of polycomplexes in *Δhtp-3 syp-4(ie25)* in
254 EM is reminiscent of the architecture of SCs in *syp-4(ie25)* determined by 3D-STORM. These
255 findings indicate that structural defects within polycomplexes are sufficient to alter special
256 patterning of CO proteins, analogous to the structurally altered SCs that assemble in *syp-4(ie25)*
257 mutants.
258
259 **Discussion**
260 Together these findings establish that the correct organization of the synaptonemal
261 complex is required for spatial patterning of crossovers, and further corroborate previous
262 findings that the SC is important for crossover interference. They further suggest that CO
263 regulation may involve transduction of structural information through this liquid crystalline
264 material. This idea is reminiscent of a "beam-film" model for crossover interference, which
265 proposes that crossovers relieve local stress along a beam-like material [49, 51]. This mechanical
266 stress has been proposed to be imposed by chromatin structure and/or tethering of chromosomes;
267 however, our findings reinforce previous studies that implicated the SC as a crucial mediator of
268 crossover patterning [8, 9, 12]. In particular, we have reported that polycomplexes comprised of
269 SC central region proteins alone can mediate spatial patterning of GFP-COSA-1 foci even in the
270 absence of association with chromatin or axis proteins, and polycomplexes in *syp-4(ie25)*
271 mutants exhibit both defects in their internal organization and altered patterning of GFP-COSA-1

foci. Interestingly, forces applied to nematic liquid crystalline materials such as the SC [3] can perturb the orientation of molecules within the liquid crystal [35]. Therefore, we speculate that the reorganization of proteins within the SC that occurs concomitant with CO designation may reflect a mechanical signaling component of CO interference.

Figures

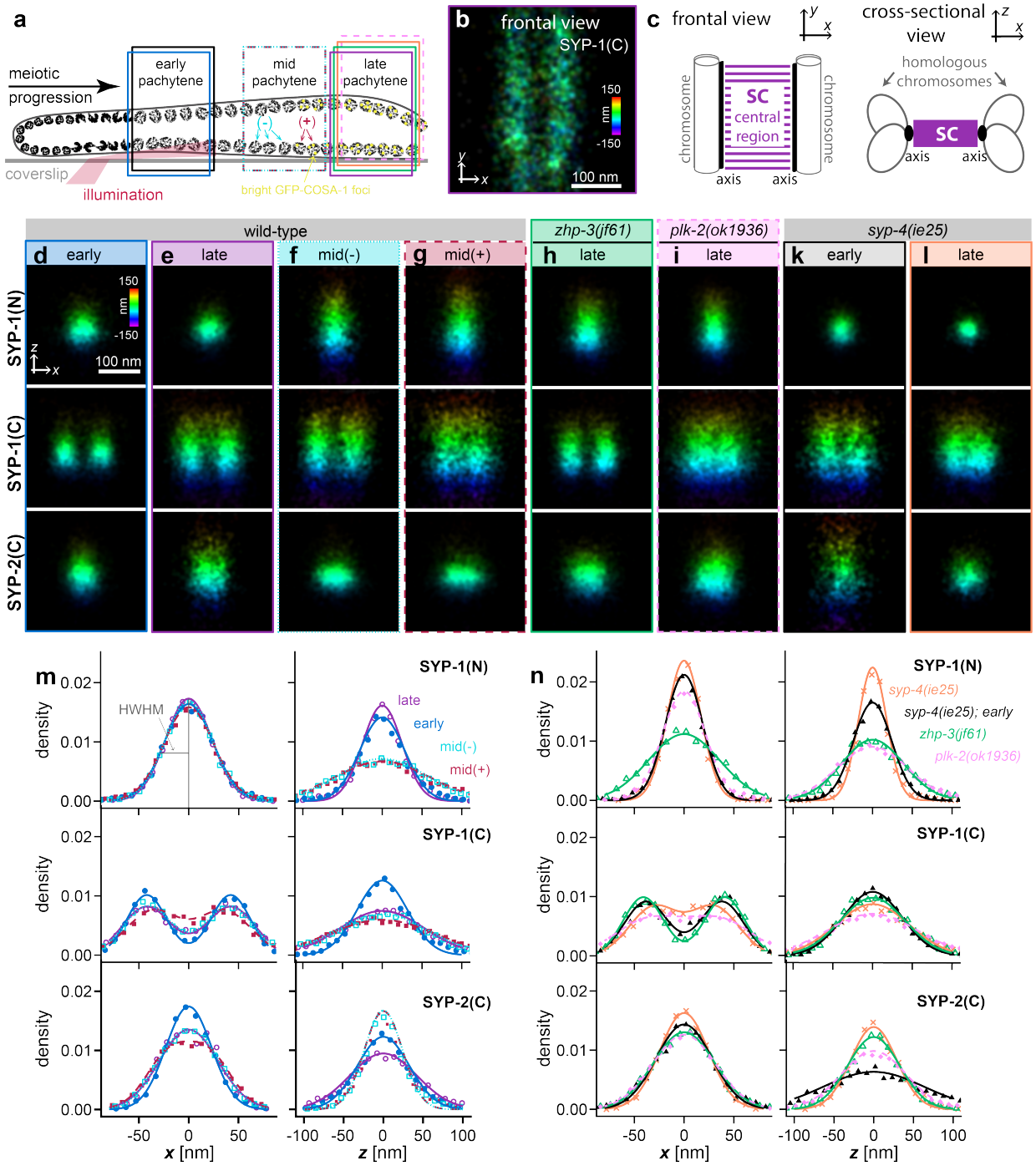

Figure 1: Super-resolution microscopy reveals the dynamic three-dimensional organization of the synaptonemal complex. (a) In the *C. elegans* gonad, nuclei (representative DAPI images) are arranged in a gradient of premeiotic and meiotic stages. Using highly inclined illumination

(red), we imaged SCs in the bottom section of nuclei adjacent to the coverslip (gray) in early, mid- and late pachytene (rectangles). Mid(-) (cyan) and mid(+) (red) pachytene correspond to nuclei without and with bright GFP-COSA-1 foci in the same field of view, respectively. (b) Measurements based on averaged STORM images indicate that the C-terminus of SYP-1 lies close to the chromosome axes. Colors denote localizations in *z* from -150 to 150 nm (color scale bar). (c) The schematic depicts the SC, which forms a ladder-like structure approximately 100-nm wide (purple), which links the axes (black) of paired homologous chromosomes (white rods) in the frontal view (left). To visualize the 3D architecture of the SC, we show cross-sectional views of the SC as depicted (right). (d-l) Averaged cross-sectional views of STORM images for the N-terminus of HA-SYP-1 (top row), the C-terminus of SYP-1 (center row), and C-terminus of SYP-2 (bottom row), for wild-type SCs in early (d, blue closed spheres in m), late (e, purple closed spheres in m), mid(-) (f, cyan open squares in m), and mid(+) (g, red closed squares in m) pachytene and for *zhp-3(jf61)* (h, green triangles, late pachytene in n), *plk-2(ok1936*) (i, pink diamonds in n, late pachytene) and *syp-4(ie25)* (k, black closed triangles for early pachytene orange crosses in late pachytene in n). (m, n) Histograms of localization events in frontal view (*x*, left) and across the SC (*z*, right) are fitted with 1 or 2 Gaussians. The results of the fits are summarized in Extended Data Table S1.

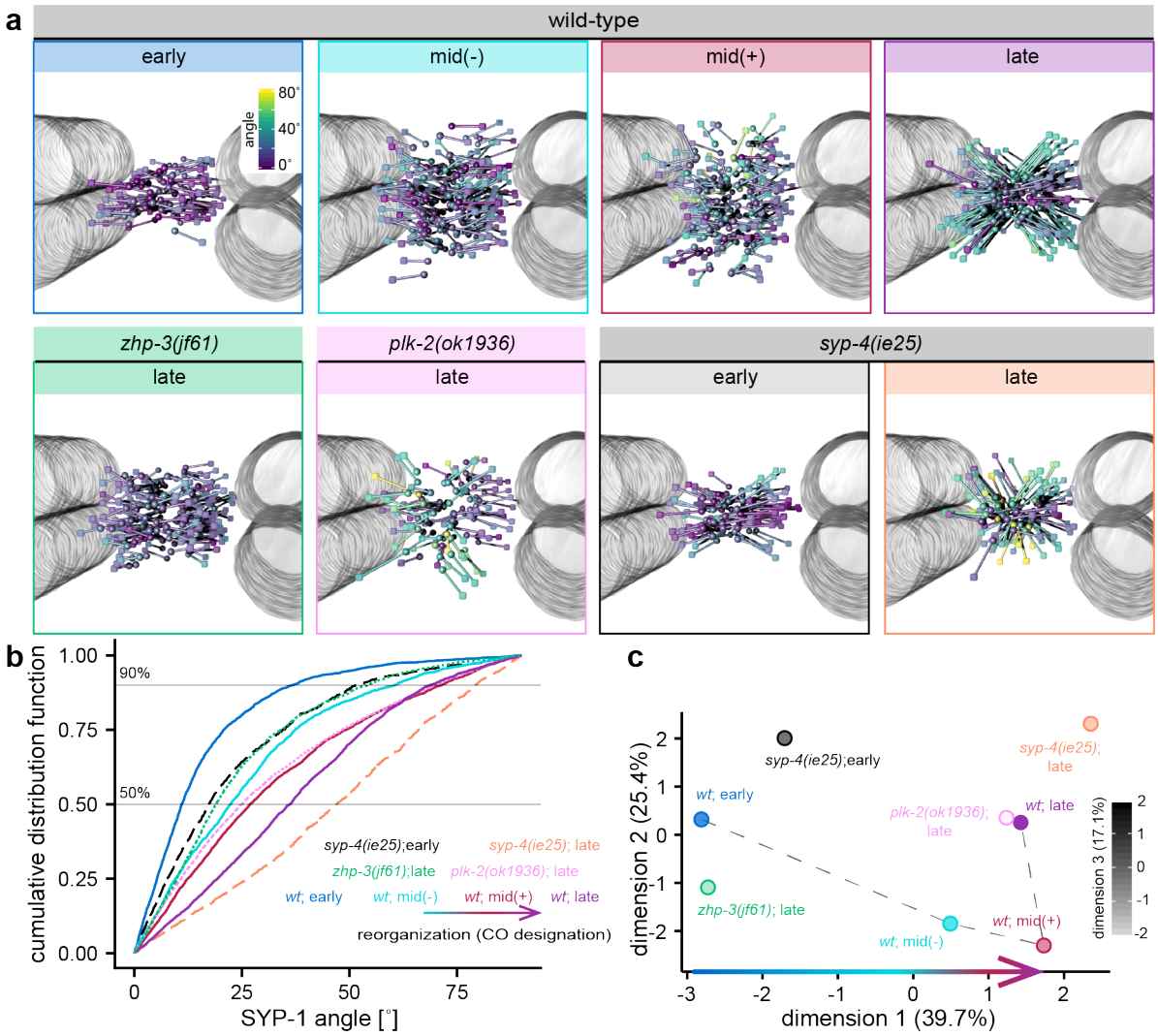

Figure 2: The synaptonemal complex undergoes a structural transition upon crossover designation. (a) The stochastic nature of STORM does not allow us to image the N- and C-terminus of a specific single molecule at the same time but will yield population averages for the localization of individual domains. We therefore used a probabilistic mapping approach to reconstruct the orientation of SYP-1 molecules for each condition and genotype. The resultant models of SYP-1 (black) are shown with C-termini depicted as cubes and N-termini as spheres. A proxy for chromatin (gray areas) is added for visualization purposes. Models are rendered using POV-ray (v3.7.0). Models show changes in the orientation of SYP-1 upon crossover formation. (b) These changes are revealed by the distributions of angles of SYP-1 with respect to the central plane of the SC in cross-sectional views. Cumulative distribution functions are shown. Gray horizontal lines mark median (50%) and 90th percentile values. (c) A principal component analysis (see methods) summarizes the SC organization at different conditions and

genotypes. The progression of SC reorganization in wild-type animals throughout pachytene is highlighted by a gray dashed line. Dimension 1 scales with SC reorganization upon crossover formation (colored arrow). We note that mid(-) SCs prior to designation of COs marked by bright GFP-COSA-1 foci are closer to late pachytene than early pachytene. This suggests that some aspects of the transition in SC reorganization may occur even prior to the appearance of GFP-COSA-1 foci and/or nuclei designated mid(-) pachytene may include false negatives given that our field of view in *z* is limited to 1 µm slices and does not contain whole nuclei. SC organization in late pachytene *zhp-3(jf61)* mutants that lack CO formation is similar to wild-type early pachytene, while SCs in *plk-2(ok1936)* null mutants resemble wild-type SCs. By contrast, SCs in *syp-4(ie25)* mutants are distinct in both early and late pachytene.

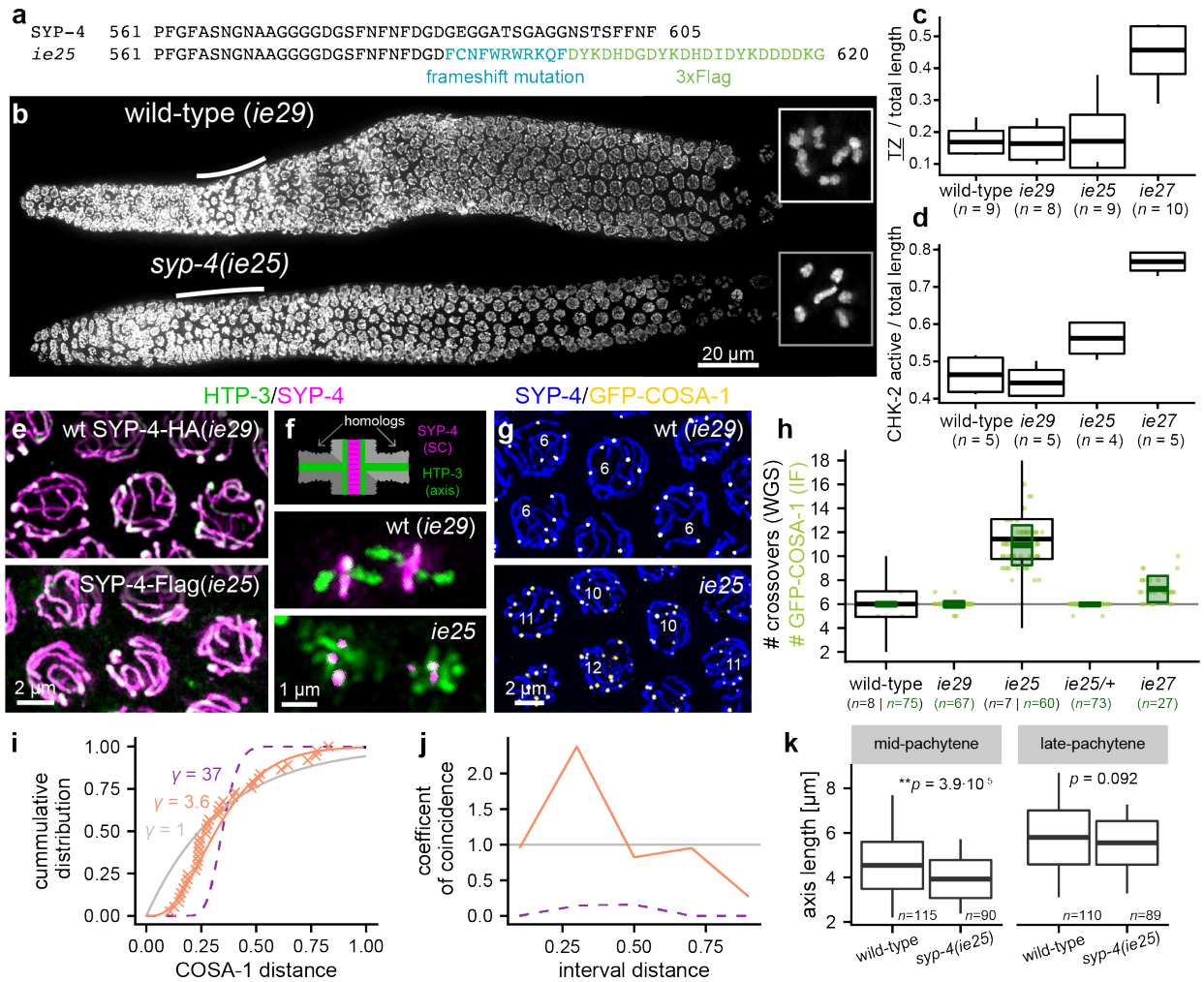

Figure 3: Crossover interference is diminished in *syp-4(ie25)* mutants. (a) The C-terminal amino-acid sequences of wild-type SYP-4 and SYP-4(*ie25*) are indicated. (b) Fluorescence micrographs of DAPI-stained gonads from wild-type (*syp-4-ha(ie29)*, top) and *syp-4(ie25)* mutants (bottom). Insets depict single oocyte nuclei, revealing 6 bivalents in both wild-type and *syp-4(ie25)*. (c) The *syp-4(ie25)* mutation or epitope tagging of *syp-4* alone *(ie29)* did not perturb the length of the transition zone (solid lines in b), but this length was significantly increased in *syp-4-ha(ie27)* mutants, indicative of a defect in synapsis. (d) Immunofluorescence detection of a CHK-2-dependent phoshpoepitope provides a more consistent assay for meiotic progression. In animals homozygous for the syp-4-HA allele *ie29,* this "CHK-2 active" zone comprises 45% of the length of the germline containing leptotene, zygotene and pachytene stages of meiosis. This fraction was extended to 56% and 77% in *ie25* and *ie27*, respectively. Boxplots in c and d show mean±s.d (whiskers show minima and maxima). (e) Fluorescence micrographs reveal robust synapsis for *ie29* (top) and *ie25* (bottom). (f) The cruciform bivalent structure, as illustrated in the cartoon (top) is disrupted in *ie25*, likely reflecting the occurrence of multiple crossovers per

chromosome pair. Immunostaining of HTP-3 (axis; green) and SYP-4 (SC; magenta) is shown (e-f). (g) The number of crossovers per nucleus as estimated from whole genome sequencing (black/white boxplots, mean±s.e., whiskers are extreme values) correspond to the number of GFP-COSA-1 foci (green dots and boxplots, mean±s.d.). (h) Fluorescence micrographs show a marker for designated crossovers, GFP-COSA-1 (yellow), and SYP-4 (blue). (i) To measure crossover interference strength, we fit the cumulative distribution function of inter-GFP-COSA-1 distances in *syp-4(ie25)* mutants (orange crosses) using a gamma function[44]. γ=1 denotes no interference (gray), γ=37 corresponds to interference measured for wild-type animals[9] (purple dashed line), while interference in *syp-4(ie25)* is severely reduced to γ=3.5 (orange line, n=41 chromosomes). (j) Likewise, interference strength can be described by the coefficient of coincidence[45], which denotes the ratio of the observed number of 2 COs (GFP-COSA-1 foci) at a given distance to the expected number assuming random CO distribution. In wild-type animals, the coefficient of coincidence of GFP-COSA-1 foci is 0 corresponding to complete interference (purple dashed line; n=88 chromosomes), while it is approximately 1 in *syp-4(ie25)* mutants (orange, n=41), indicating no interference (gray line). (k) Chromosome axes lengths are shorter in *syp-4(ie25)* mutants compared to wild-type axes in mid(-)-pachytene prior do designation of CO sites (left) and comparable in late pachytene (right). Boxplots show mean±s.d and whiskers are extreme values.

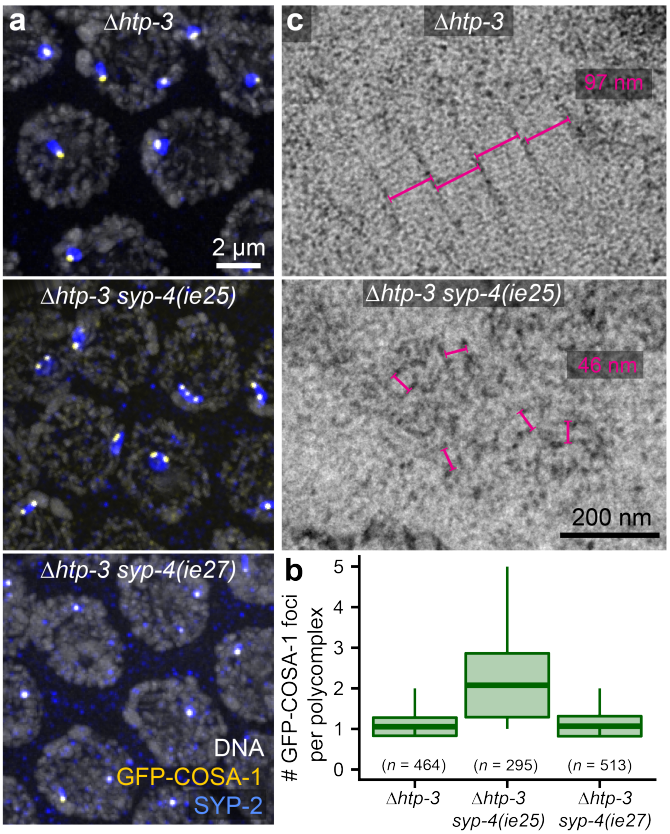

Figure 4: Irregular organization and an increase in GFP-COSA-1 foci in *syp-4(ie25)* polycomplexes. (a) Fluorescence micrographs show that the number of GFP-COSA-1 foci (yellow) is limited to 1 or 2 per polycomplex (SYP-2, blue) in wild-type conditions (Δ*htp-3*) and in the presence of *syp-4(ie27)* but is elevated in *syp-4(ie25)*. DAPI is shown in gray. (b) Quantification of GFP-COSA-1 foci. Boxplots show mean±s.d. and whiskers are extreme values. (c) Representative electron micrographs show that the SC-like structure of polycomplexes (Δ*htp-3*, 97 nm spacing of parallel, electron dark regions) is disturbed in Δ*htp-3 syp-4(ie25)*, which are disorganized and 46 nm apart.

375 **Table S1: Summary of localizations of SC components determined by STORM.** Positions
376 are distances of the maxima to the center of the SC (wt = wild-type; early = early pachytene;
377 mid(-) = mid pachytene nuclei without bright GFP-COSA-1 foci; mid(+) = mid pachytene nuclei
378 with bright GFP-COSA-1 foci). HWHM denotes the half width at half maximum of the
379 distributions (Fig. 1m, gray lines)

domain	condition	x [nm]		z [nm]		total length analyzed [nm] (# images)
		position	HWHM	position	HWHM	
HA-SYP-1	wt, early	0	28.3 ± 1.8	0	33.1 ± 2.7	3438 (8)
	wt; mid(-)	0	27.5 ± 1.6	0	65.4 ± 2.8	3056 (5)
	wt; mid(+)	0	29.4 ± 2.6	0	69.7 ± 3.5	3992 (6)
	wt, late pachytene	0	27.0 ± 1.6	0	29.1 ± 3.7	4780 (9)
	zhp-3(jf61)	0	42.7 ± 2.5	0	46.9 ± 2.9	3579 (7)
	plk-2(ok1936)	0	25.5 ± 1.5	0	52.0 ± 3.9	4136 (10)
	syp-4(ie25); early	0	22.1 ± 1.4	0	28.6 ± 1.2	4351 (10)
	syp-4(ie25); late	0	19.8 ± 0.8	0	20.5 ± 1.6	3114 (6)
SYP-1(C)	wt, early	42.3 ± 0.8	22.8 ± 0.9	0	37.1 ± 2.3	4092 (7)
	wt; mid(-)	40.8 ± 1.3	28.2 ± 0.6	0	68.1 ± 4.3	3184 (7)
	wt; mid(+)	35.9 ± 0.9	31.2 ± 1.0	0	78.7 ± 2.8	3503 (7)
	wt, late pachytene	42.0 ± 1.2	28.5 ± 1.0	0	62.7 ± 3.2	5312 (9)
	zhp-3(jf61); late	41.0 ± 1.3	23.6 ± 1.1	0	48.2 ± 4.3	1851 (8)
	plk-2(ok1936); late	36.3 ± 1.4	39.6 ± 3.6	0	67.0 ± 2.5	5741 (9)
	syp-4(ie25);	38.5 ± 2.5	24.9 ± 0.8	0	43.2 ± 3.8	2768 (5)

	early					
	syp-4(ie25); late	30.5 ± 1.5	29.1 ± 1.8	0	54.0 ± 2.2	4848 (6)
SYP-2(C)	wt, early	0	27.0 ± 2.0	0	38.3 ± 3.7	5866 (10)
	wt; mid(-)	16.3 ± 7.5	27.1 ± 2.7	0	27.6 ± 1.1	8437 (9)
	wt; mid(+)	20.6 ± 6.3	26.5 ± 3.6	0	27.7 ± 1.4	8615 (12)
	wt, late pachytene	18.9 ± 2.1	21.6 ± 1.5	0	49.5 ± 5.0	4573 (9)
	wt, late (HA)	20.9 ± 0.9	20.0 ± 1.3	0	39.9 ± 2.6	2958 (8)
	zhp-3(jf61); late	0	36.1 ± 4.3	0	38.6 ± 3.8	3746 (6)
	plk-2(ok1936); late	0	37.1 ± 2.0	0	47.4 ± 2.3	8206 (9)
	syp-4(ie25); early	0	32.4 ± 2.2	0	73.6 ± 8.8	3172 (7)
	syp-4(ie25); late	0	28.9 ± 2.7	0	33.4 ± 3.2	3604 (8)
GFP-SYP-3	wt, early	0	23.3 ± 0.8	0	40.0 ± 4.5	1784 (4)
	wt, late pachytene	0	18.5 ± 1.4	0	63.2 ± 6.2	2238 (6)
SYP-3-HA	wt, early	12.3 ± 1.8	20.3 ± 1.2	0	27.1 ± 2.4	4653 (10)
	wt, late pachytene	16.6 ± 4.7	29.0 ± 2.3	0	48.1 ± 5.9	2764 (7)
	zhp-3(jf61); late	14.2 ± 2.0	24.4 ± 1.4	0	28.5 ± 2.2	2723 (6)
SYP-4-intFlag	wt, early	0	25.8 ± 0.9	0	43.3 ± 5.3	3462 (9)
	wt, late pachytene	0	30.3 ± 4.3	0	49.8 ± 4.6	2524 (4)
SYP-4-HA	wt, early	14.2 ± 2.0	23.0 ± 1.6	0	38.6 ± 2.4	5355 (10)

	wt, late pachytene	0	36.8 ± 1.1	33.1 ± 11.9	51.5 ± 8.0	5264 (9)
SYP-4(*ie25*)	syp-4(ie25); late	0	29.1 ± 1.1	0	54.9 ± 5.6	4611 (9)
HIM-3	wt, early	33.5 ± 5.2	43.4 ± 2.3	n.d.	n.d.	2548 (6)
	wt, mid(-)	41.4 ± 2.2	46.7 ± 1.8	n.d.	n.d.	3661 (7)
	wt, mid(+)	41.8 ± 1.9	45.1 ± 1.2	n.d.	n.d.	2817 (7)
	wt, late pachytene	47.3 ± 1.5	30.2 ± 1.2	n.d.	n.d.	4411 (11)
	zhp-3(jf61); late	45.9 ± 1.6	49.0 ± 2.3	n.d.	n.d.	6969 (11)
	plk-2(ok1936); late	41.5 ± 3.8	53.9 ± 4.1	n.d.	n.d.	4769 (8)
	syp-4(ie25); early	45.3 ± 3.6	48.9 ± 2.7	n.d.	n.d.	3900 (7)
	syp-4(ie25); late	35.8 ± 3.8	45.9 ± 3.1	n.d.	n.d.	2926 (6)

385 **Table S2: List of Strains used in this study and their characterization.** *p*-Values for deviation
386 from wild-type are calculated using Mann-Whitney tests.
387

name	genotype	egg viability [%] (*p*-value)	males [%] (*p*-value)	# of eggs
N2	*wild-type*	104±6	0.08±0.20	4773
GFP-COSA-1 [36]	*meIs8* II	107±4	0.00±0.00	1362
mEos-HIM-3 [24]	*meIs8* II; *him-3(ie33)* IV	n.d.	n.d.	
mMaple-HIM-3 [24]	*meIs8* II; *him-3(ie34)* IV	n.d.	n.d.	
HA-SYP-1	*meIs8* II; *him-3(ie33)* IV; *syp-1(ie40[syp-1(1-47)::HA::syp-1(48-489)])* V	100±4 (0.886)	0.00±0.00 (0.452)	840
SYP-2-HA	*meIs8* II; *him-3(ie33)* IV; *syp-2(ie99[syp-2::HA])* V	101±6 (0.394)	0.00±0.00 (1.00)	1405
GFP-SYP-3	*syp-3(ok758)* I; *ieSi11 [syp-3p::syp-3::EmGFP::syp-3-3'UTR + unc-119(+)]* II; *him-3(ie33)* IV	83±10 (0.031)	0.87±0.59 (0.045)	1143
SYP-3-HA	*syp-3(ie42[syp-3::HA])* I; *meIs8* II; *him-3(ie33)* IV	95±4 (0.041)	1.80±0.60 (0.004)	1457
SYP-4-HA(*ie29*)	*syp-4(ie29[syp-4::HA])* I; *meIs8* II; *him-3(ie34)* IV	100±2 (0.150)	0.72±0.41 (0.052)	1336
SYP-4-HA(*ie29*)	*syp-4(ie29[syp-4::HA])* I; *meIs8* II	105±3 (0.686)	0.00±0.00 (1.000)	951
SYP-4-intFlag	*syp-4(ie30[syp-4(1-315)::2xFlag::syp-4(319-605)])* I; *meIs8* II; *him-3(ie33)* IV	98±3 (0.032)	1.91±0.59 (0.010)	1350
SYP-4(*ie25*)	*syp-4(ie25[syp-4ΔC::3xFlag])* I; *meIs8* II	38±4 (0.008)	5.97±1.25 (0.010)	1024
SYP-4-HA(*ie27*)	*syp-4(ie29[syp-4::HA::mod3'UTR])* I; *meIs8* II	80±9 (0.002)	1.58±1.58 (0.010)	992
Δ*htp-3* [3]	*htp-3(tm3655)* I; *meIs8* II	n.d.	n.d.	
Δ*htp-3 syp-4(ie25)*	*htp-3(ie100) syp-4(ie25)* I; *meIs8* II	n.d.	n.d.	

Δ*htp-3 syp-4(ie27)*	*htp-3(ie101) syp-4(ie27)* I; *meIs8* II	n.d.	n.d.	
SYP-4(*ie25*)	*syp-4(ie25[syp-4ΔC::3xFlag])* I; *meIs8* II; *him-3(ie33)* IV	n.d.	n.d.	
SYP-4(*ie25*); HA-SYP-1	*syp-4(ie25)* I; *meIs8* II; *him-3(ie33)* IV; *syp-1(ie40)* V	n.d.	n.d.	
zhp-3(jf61)	*zhp-3(jf61)* I; *meIs8* II; *him-3(ie33)* IV	n.d.	n.d.	
***zhp-3(jf61)*; HA-SYP-1**	*zhp-3(jf61)* I; *meIs8* II; *him-3(ie33)* IV; *syp-1(ie40)* V	n.d.	n.d.	
***zhp-3(jf61)* SYP-3-HA**	*syp-3(ie102[syp-3::HA]) zhp-3(jf61)* I; *meIs8* II; *him-3(ie33)* IV	n.d.	n.d.	
***plk-2(ok1936);* HA-SYP-1**	*plk-2(ok1936)* I; *meIs8* II; *him-3(ie33)* IV; *syp-1(ie40)* V	n.d.	n.d.	

388
389

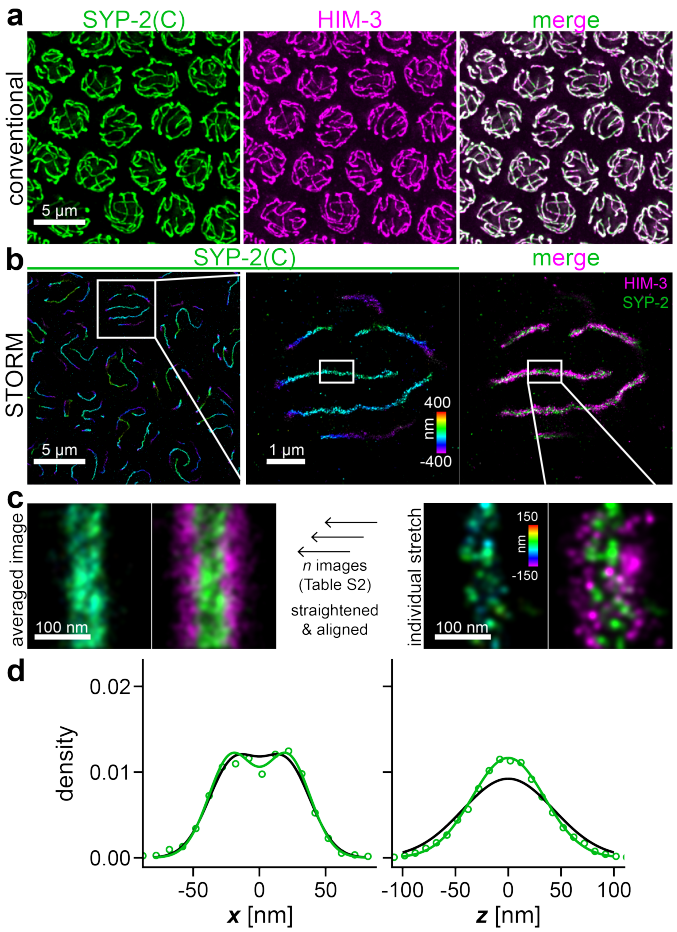

Extended Data Figure S1: Experimental strategy for mapping the architecture of the synaptonemal complex. (a) The resolution in conventional fluorescence micrographs is insufficient to visualize the structure of the axis or SC (HIM-3, magenta, left) and SC components (SYP-2-HA, green, center) are co-localized (merge, right). (b) The structure of the SC is resolved by STORM super-resolution microscopy. Colors denote localization in *z* (left and center). Localization of HIM-3 (magenta, right) is used to determine the orientation of the SC (SYP-2-HA(C), wild-type, late pachytene in green). White boxes in b show regions magnified in other panels. (c) For further analysis, individual stretches in frontal view (right), which are characterized by clearly separated HIM-3 axes, are straightened and aligned in *x* and *z* to generate the averaged image (left). (d) The results are highly reproducible between different preparations and different antibodies (SYP-2(C) peptide antibody, black, and SYP-2-HA epitope antibody, green) (Table S2). Note that the widths of the distributions are narrower for the monoclonal HA antibody compared to the polyclonal SYP-2(C) peptide antibody.

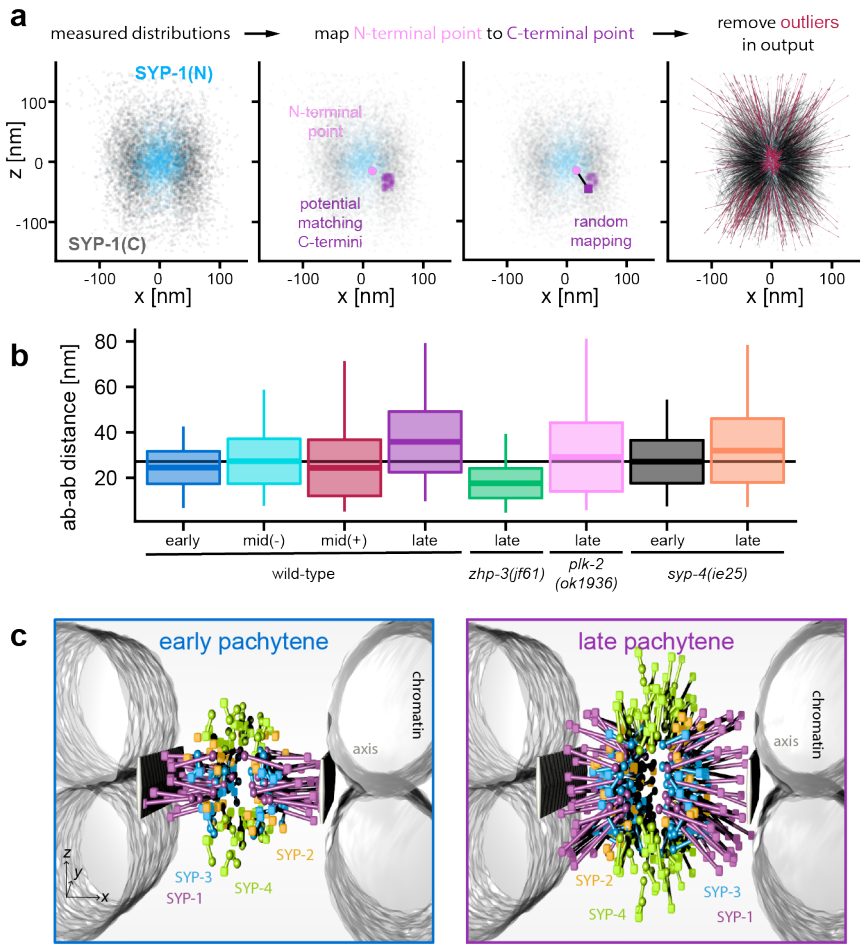

Extended Figure S2: Dynamic orientation of SYP-1 molecules. (a) To generate a model of SYP orientation within the SC, individual datapoints (magenta circle, center) in the measured distributions of the N- (blue, left) and C-terminus (gray, left) of a given component (here: SYP-1 in wild-type late pachytene) are randomly mapped to a localization event within the same percentile ±7.5% tolerance of the C-terminal distribution in *x* and *z* (purple, center). Mapped events resulting in the shortest or longest 5% of antibody to antibody distances (red, right) are disregarded. (b) The boxplots show means±s.d. of the distances between N- and C-terminal antibodies as estimated by the probabilistic mapping approach. Whiskers are extremes and the black line shows the mean across all genotypes and conditions. (c) The resultant model of SC organization generated by mapping of N- and C-terminal distributions of SYP proteins is shown for early (left) and late (right) pachytene in wild-type animals. C-termini are cubes and N-termini

418 (central domain for SYP-4) are spheres. The localization of HIM-3 in *x* is used as a proxy for
419 axis localization. Models are rendered using POV-ray (v3.7.0).
420
421

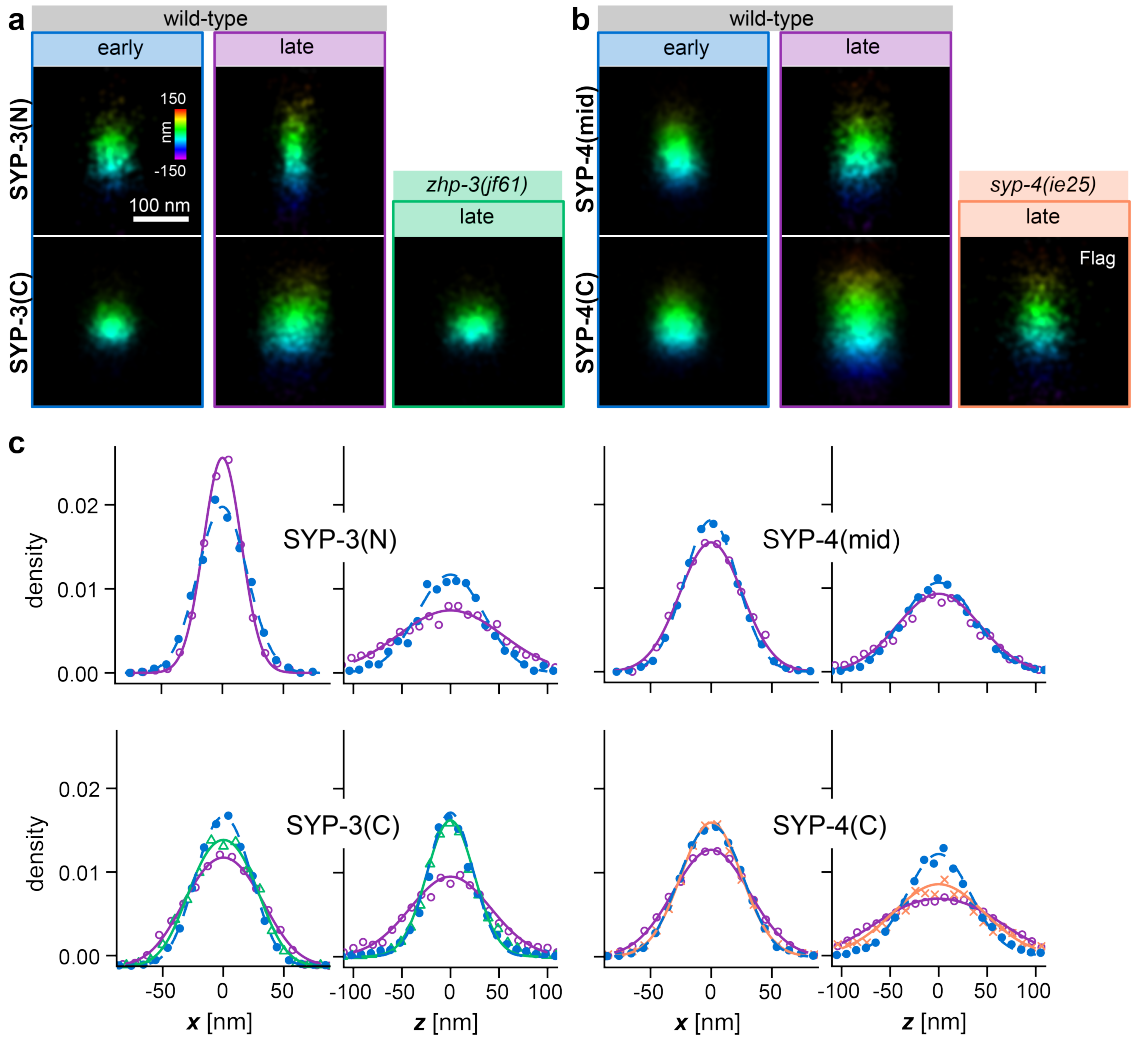

Extended Data Figure S3: Dynamic organization of SYP-3 and SYP-4 within the SC. (a-b) Averaged STORM images show cross-sectional views of SYP-3 (a) and SYP-4 (b) domains as indicated in wild type at early (blue) and late pachytene (purple) and *zhp-3(jf61)* (orange) and *syp-4(ie25)* (green) mutants in late pachytene. Colors denote localization in *z*. The distributions of localization events in frontal (*x*), and vertical (*z*) views are analyzed in (c). The results are summarized in Extended Data Table S2.

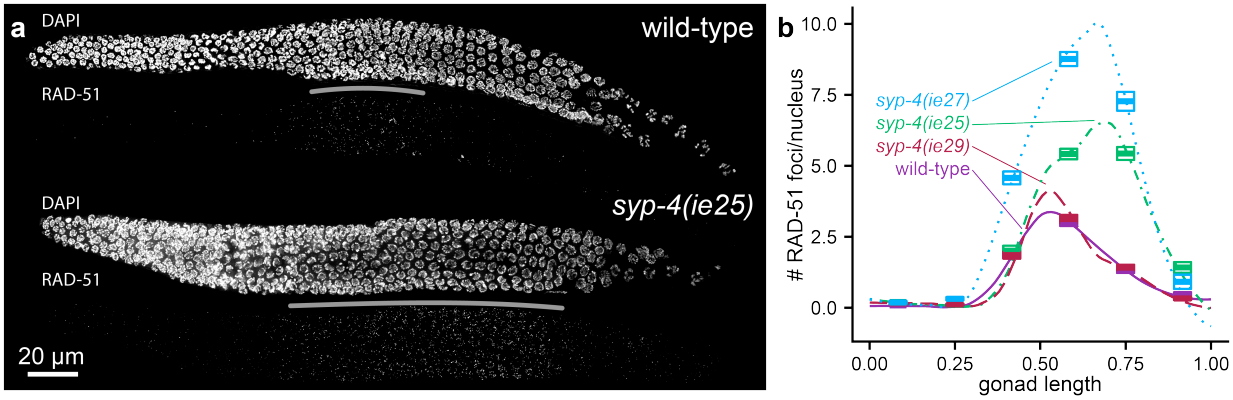

Extended Data Figure S4: Double-strand break formation is extended in *syp-4(ie25)*. (a) Immunofluorescence images show DAPI (upper) and RAD-51 (lower), which marks double-strand breaks. While the RAD-51 zone (gray line) is normally limited to a short region in early/mid-pachytene in wild-type (top), it is markedly elongated in *syp-4(ie25)* (bottom). (b) shows the average number of RAD-51 foci per nucleus (boxes are mean±s.e.) as a function of the relative length of the gonad from the distal tip to the end of pachynema of wild-type (purple solid line, *n*=1672 nuclei from (7) gonads), *syp-4(ie29)* (red dashed line, *n*=1407 (6)), *syp-4(ie25)* (green dot-dashed line, *n*=1440 (6)) and *syp-4(ie27)* (blue dotted line, *n*=1162 (4)), respectively.

447

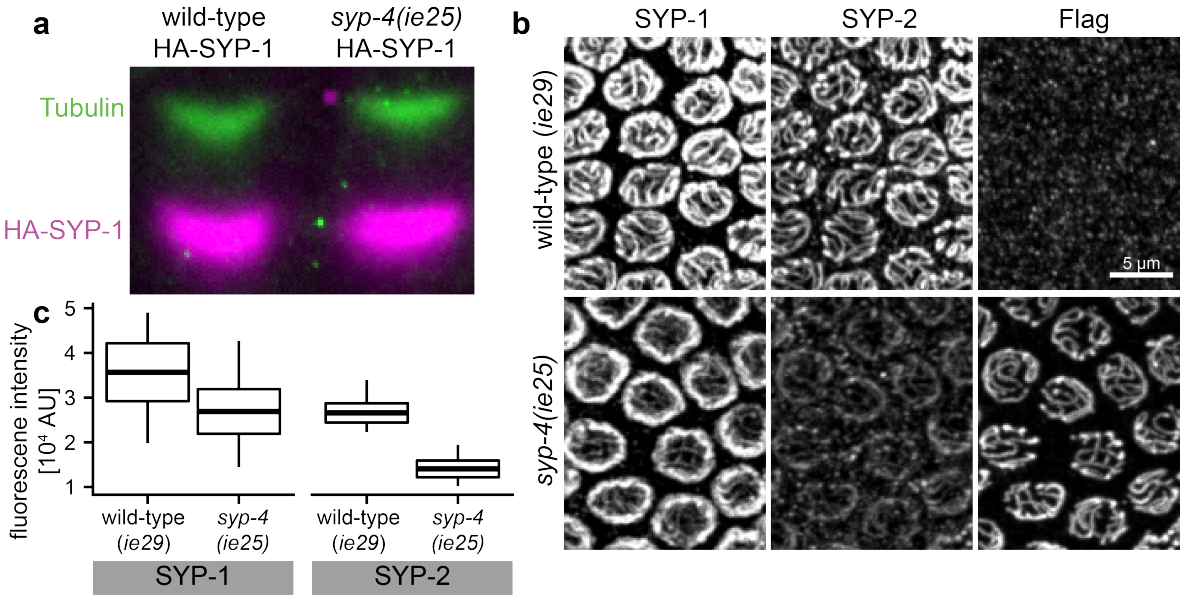

448

449 **Extended Data Figure S5: Abundance of SC proteins in *syp-4(ie25)*.** (a) The expression level
450 of HA-SYP-1 (magenta) is identical in wild-type and *syp-4(ie25)* strains as shown by a Western
451 Blot. Tubulin (green) is shown as a reference. (b) By contrast, the levels of immunofluorescence
452 staining for SYP-1 (left) and SYP-2 (center) are drastically reduced in *syp-4(ie25)* SCs (bottom)
453 compared to wild-type (*syp-4-ha(ie29)*, right). To ensure identical handling, gonads from both
454 genotypes were stained in a single reaction and their genotype was determined by anti-Flag
455 staining (right), which marks *syp-4(ie25)* but not *syp-4(ie29)*. (c) Boxplots show mean±s.d.
456 (whiskers are extreme values) of fluorescence intensities of late pachytene SCs (*ie29*: *n*=339,
457 *ie25*: *n*=209).

458

459

460

461

462

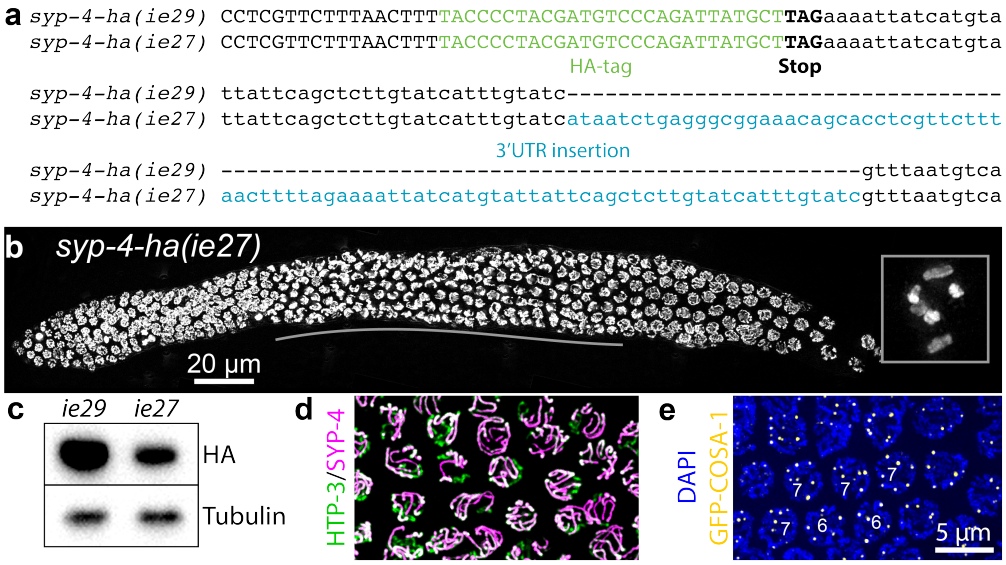

463

464 **Extended Data Figure S6: The *syp-4-ha(ie27)* mutation phenocopies partial RNAi of other**
465 **SC components.** (a) The mutation *syp-4-ha(ie27)* (bottom) is constituted by an insertion (cyan)
466 in the 3' untranslated region (lower case letters) of the *syp-4* gene, but the coding sequence
467 (capital letters) is identical to *syp-4-ha(ie29)* (top), which is phenotypically wild-type. (b) A
468 DAPI stained fluorescence micrographs show that meiotic progression is delayed in *syp-4-*
469 *ha(ie27)* as indicated by an elongated transition zone (gray line) but can form 6 bivalents (inset)
470 indicating largely successful homologous pairing and crossover formation. (c) A western blot
471 shows that the level of SYP-4-HA (top) is reduced to ~ 30 % in *syp-4-ha(ie27)* compared to *syp-*
472 *4-ha(ie29)*. Tubulin is shown as a reference (bottom). (d) Synapsis is delayed in *syp-4-ha(ie27)*
473 as shown by the incomplete overlap of immunofluorescence images of an axial protein (HTP-3,
474 green) and SC proteins (SYP-4-HA, magenta). (e) As has been described for partial RNAi
475 depletion of SYP-1, -2 and -3[9], a reduction in SYP-4 expression level results in a slight
476 increase in the number of GFP-COSA-1 (yellow) foci to about 7 foci/nucleus (DAPI is shown in
477 blue).

478

479

Methods

Worm strains and transgenes

A complete list of *C. elegans* strains used in this study can be found in Table S1. All strains were cultured at 20ºC using standard methods[52]. GFP-SYP-3[32] was inserted by MosSCI[53] and crossed into *syp-3(ok758)*. Other tags were inserted using CRISPR-Cas9 genome editing as described in[24]. Briefly, Cas9 and gRNA were delivered by microinjection, either encoded on a plasmid[54] or as *in vitro* preassembled Cas9-ribonucleoprotein complexes. Repair templates for small epitope tags were codon optimized for *C. elegans* [55] and synthesized as "Ultramers" by IDT.

Immunofluorescence

Immunofluorescence of dissected gonads from young adults 24 h post L4 was performed as described[56] with modifications described in[24]. The following primary antibodies, all of which have been previously described, were used: goat anti-SYP-1 (1:500, affinity purified)[37], mouse anti-HA (1:500, monoclonal 2-2.2.14, Thermo Fisher Scientific), rabbit anti-SYP-2 (1:500, affinity purified)[16], mouse anti-GFP (1:500, monoclonal 7.1 and 13.1, Roche), mouse anti-Flag (1:500, monoclonal M2, Sigma-Aldrich), chicken anti-HTP-3 (1:500)[57], rabbit anti-HIM-3 (1:500, SDQ4713 ModENCODE project)[58], rabbit anti-HIM-8pT64 (1:2000)[41], and rabbit anti-RAD-51 (1:500)[37]. Secondary antibodies raised in donkeys were fluorescently labelled with Alexa Fluor® 488, Cy3 or Alexa Fluor® 647 (1:500, Jackson ImmunoResearch and Invitrogen). Gonads were mounted in ProLong Gold antifade mountant (ThermoFisher Scientific) and epifluorescence images were acquired on a DeltaVision Elite microscope (Applied Precision) using a 100× N.A. 1.4 oil-immersion objective.

For quantification of proteins levels by immunofluorescence, imaging was performed on a Marianas spinning-disk confocal microscope (3i) with a 100x 1.46 NA oil immersion objective. 3D stacks of wild-type (*syp-4-ha(ie29)*) and *syp-4(ie25)* animals were taken from the same slide and quantified in Fiji. SC containing voxels are identified by thresholding the SYP-2 and SYP-4-3xFlag channels for *syp-4(ie29)* and *syp-4(ie25)*, respectively. Images shown in Fig. S6 are background subtracted maximal intensity projections with equally scaled intensity values.

STORM and PALM imaging

511 Super-resolution imaging of dissected, immuno-stained intact germline tissue was carried out as
512 described[24]. Targets for STORM were labeled with donkey or goat secondary antibodies
513 labelled with Alexa Fluor® 647 (1:500, Jackson ImmunoResearch and Invitrogen).
514 Subsequently, the fluorescently tagged internal reference protein, mEos2-HIM-3 or mMaple3-
515 HIM-3[24] was imaged using PALM [59] [60]. For early pachytene images, mEos2-HIM-3 was
516 co-stained with a rabbit anti-HIM-3 antibody and a donkey-anti-rabbit secondary antibody
517 (Jackson ImmunoResearch) labelled with NHS esters of CF568 to achieve a 2:1 dye-to-antibody
518 ratio. Aligned and averaged images (Fig. S1) were used to generate histograms of localization
519 events in *x* and *z*[24]. To systematically distinguish between mono- and bi-modal distributions,
520 we evaluated fits with one and two Gaussians using an ANOVA test in R ($p < 0.05$). Standard
521 deviations of fit parameters were estimated by a subsampling approach using subsets of half the
522 number of individual SC stretches[24]. The results are summarized in Table S2.
523
524 **Statistical analysis**
525 Sample sizes were not predetermined, and experiments were not randomized. The investigators
526 were not blinded to allocation during experiments and outcome assessment. For STORM
527 experiments, the total lengths and number of stretches analyzed are summarized in Table S2.
528
529 **Analysis of of SC organization**
530 To derive a model for SC organization from our data, we asked which orientations of SC
531 proteins were consistent with the observed distributions, assuming that each protein is a rigid
532 rod. We first corrected the raw data by removing the extreme 2.5% of the localization events
533 using squared Mahalanobis distances in R (version 3.4.2). We then mapped each localization
534 event corresponding the *n*th-percentile in *x* and the *m*th-percentile in *z* of the N- (or C-) terminal
535 distribution to a randomly selected localization event within the *n*th ± 7.5% in *x* and *m*th ± 7.5%
536 in *z* of the corresponding C- (or N-) terminal distribution. This analysis reveals the distance
537 between the N- and C-terminal antibodies used for imaging and the orientation of the protein
538 within the SC. For further analysis, we remove outliers among the mapped localization events
539 with extreme values corresponding to the lower and upper 2.5% of distances.
540 To visualize changes within SC organization, we performed principal component analysis of the
541 widths, and – where applicable – positions off-center, for N- and C-terminal distributions of

542 SYP-1 and the C-terminal distribution of SYP-2, the orientations of SYP-1 molecules as
543 characterized by the median and 90th percentile angles, and the average distance between N- and
544 C-terminal antibodies using R (version 3.4.2). We excluded SYP-3 and SYP-4 from this analysis
545 since experimental challenges prevented us from analyzing their localizations for all genotypes.
546

547 **Recombination mapping**

548 To map meiotic recombination events, the *syp-4(ie25)* allele (generated in Bristol N2
549 background) was introgressed into the divergent Hawaiian strain CB4856 by 8 sequential crosses
550 and selection for *ie25*. Hawaiian and Bristol wild-type and *syp-4(ie25)* strains were crossed, and
551 the hybrid F1 progeny were backcrossed to Hawaiian males. These cross-progeny, which have
552 Hawaiian paternal chromosomes and recombined Bristol/Hawaiian maternal chromosomes, were
553 plated individually, allowed to reproduce for one generation, and the genomic DNA of their
554 pooled progeny was extracted by phenol-chloroform extraction. Illumina sequencing libraries
555 were prepared as described in [61] and sequenced as 50 bp single reads on a HiSeq2500 Illumina
556 sequencer at the Vincent J. Coates Genomics Sequencing Laboratory at UC Berkeley, with a
557 coverage of 2-4x per individual. Reads were mapped to the genomes of Bristol (Wormbase
558 release WS230) and Hawaiian[62] strains and genotypes called using the multiplexed shotgun
559 genotyping (MSG) toolbox and default parameters[63]. Aligned sequences obtained by deep
560 sequencing have been uploaded on the NCBI SRA database under accession number
561 SRP126693. Following this analysis, crossovers in oogenesis are characterized by transitions
562 from Hawaiian/Bristol heterozygous stretches to homozygous Hawaiian stretches, and the
563 calculated number of crossovers per nucleus is twice the number of mapped crossovers in the
564 oocytes.
565

566 **Electron microscopy**

567 High-pressure freezing, freeze-substitution, sample preparation, and microscopy was performed
568 as described previously[3, 64, 65]. Images were acquired on a Tecnai 12 transmission electron
569 microscope (120 kV, FEI, Hillsboro, OR) equipped with a Gatan Ultrascan 1000 CCD camera
570 (Pleasanton, CA).
571

572 **Immunoblotting**

573 To compare expression levels of SYP proteins, 120 adult worms were lysed by boiling in 40 µL
574 Laemmli sample buffer (with β-mercaptoethanol) for about 5 min, until particulate matter was
575 not detected using a dissection stereomicroscope. Samples of whole-worm lysates were run on a
576 Nupage 4-12% polyacrylamide gradient gel and transferred to a PVDF membrane. Primary
577 antibodies were rabbit (Pierce, PA1-985, used for HA-SYP-1) or mouse anti-HA (SYP-4-HA)
578 and mouse anti-tubulin (EMD Millipore), each diluted 1:5,000. HRP-conjugated secondary
579 antibodies (Jackson Laboratory) were detected with ECL reagents (Amersham). For SYP-4-HA
580 blots, HA and tubulin were easily resolved and can be detected simultaneously. For HA-SYP-1,
581 HA was detected by HRP-anti-rabbit/ECL and tubulin is detected by Cy3-conjugated anti-mouse
582 secondary antibody (1:5,000). Images were recorded using a Chemidoc system (Bio-Rad) and
583 quantified using Fiji.
584

585 **Data Availability**

586 NGS datasets generated during the current study are available on the NCBI SRA database under
587 accession number SRP126693 (https://www.ncbi.nlm.nih.gov/sra/SRP126693). Any additional
588 data are available upon reasonable request.
589
590
591

Acknowledgements

We thank Lydia Smith and Rasmus Nielsen for assistance with recombination mapping, Kent McDonald and Reena Zalpuri for help with high-pressure freezing and electron microscopy and Ofer Rog and current members of our laboratories for helpful discussions and critical reading of the manuscript. Some nematode strains used in this work were provided by the Caenorhabditis Genetics Center, which is supported by the NIH - Office of Research Infrastructure Programs (P40 OD010440). This work was funded by a postdoctoral fellowship of the Human Frontier Science Program to SK (LT000903/2013-C), an NSF Graduate Research Fellowship (DGE 1106400) to MW, the Pew Biomedical Scholars Award and the Chan Zuckerberg Biohub to KX, and support to AFD from the National Institutes of Health (R01 GM065591) and the Howard Hughes Medical Institute.

Competing Interests

The authors declare no competing interests.

Author Contributions

SK and MW performed experiments and analyzed data. SK, MW, KX and AFD designed experiments and wrote the manuscript.

References

1. Zickler D, Kleckner N (1999) Meiotic chromosomes: integrating structure and function. Annu Rev Genet 33:603–754. doi: 10.1146/annurev.genet.33.1.603
2. Moses MJ (1968) Synaptinemal complex. Annu Rev Genet 2:363–412.
3. Rog O, Köhler S, Dernburg AF (2017) The synaptonemal complex has liquid crystalline properties and spatially regulates meiotic recombination factors. Elife 6:e21455. doi: 10.7554/eLife.21455

621 4. Voelkel-Meiman K, Moustafa SS, Lefrançois P, et al (2012) Full-length synaptonemal
622 complex grows continuously during meiotic prophase in budding yeast. PLoS Genet
623 8:e1002993. doi: 10.1371/journal.pgen.1002993
624 5. Pattabiraman D, Roelens B, Woglar A, Villeneuve AM (2017) Meiotic recombination
625 modulates the structure and dynamics of the synaptonemal complex during C. elegans
626 meiosis. PLoS Genet 13:e1006670. doi: 10.1371/journal.pgen.1006670
627 6. Machovina TS, Mainpal R, Daryabeigi A, et al (2016) A Surveillance System Ensures
628 Crossover Formation in C. elegans. Curr Biol 26:2873–2884. doi: 10.1016/j.cub.2016.09.007
629 7. Nadarajan S, Lambert TJ, Altendorfer E, et al (2017) Polo-like kinase-dependent
630 phosphorylation of the synaptonemal complex protein SYP-4 regulates double-strand break
631 formation through a negative feedback loop. Elife 6:e23437. doi: 10.7554/eLife.23437
632 8. Hayashi M, Mlynarczyk-Evans S, Villeneuve AM (2010) The synaptonemal complex shapes
633 the crossover landscape through cooperative assembly, crossover promotion and crossover
634 inhibition during Caenorhabditis elegans meiosis. Genetics 186:45–58. doi:
635 10.1534/genetics.110.115501
636 9. Libuda DE, Uzawa S, Meyer BJ, Villeneuve AM (2013) Meiotic chromosome structures
637 constrain and respond to designation of crossover sites. Nature 502:703–706. doi:
638 10.1038/nature12577
639 10. Wang K, Wang C, Liu Q, et al (2015) Increasing the Genetic Recombination Frequency by
640 Partial Loss of Function of the Synaptonemal Complex in Rice. Mol Plant 8:1295–1298. doi:
641 10.1016/j.molp.2015.04.011
642 11. Woglar A, Villeneuve AM (2018) Dynamic Architecture of DNA Repair Complexes and the
643 Synaptonemal Complex at Sites of Meiotic Recombination. Cell 173:1678–1691.e16. doi:
644 10.1016/j.cell.2018.03.066
645 12. Cahoon CK, Helm JM, Libuda DE (2019) Synaptonemal complex proteins direct and
646 constrain the localization of crossover-promoting proteins during Caenorhabditis elegans
647 meiosis. bioRxiv 523605. doi: 10.1101/523605
648 13. Zhang L, Köhler S, Rillo-Bohn R, Dernburg AF (2018) A compartmentalized signaling
649 network mediates crossover control in meiosis. Elife 7:245. doi: 10.7554/eLife.30789

650 14. Dernburg AF, McDonald K, Moulder G, et al (1998) Meiotic recombination in C. elegans
651 initiates by a conserved mechanism and is dispensable for homologous chromosome
652 synapsis. Cell 94:387–398.
653 15. MacQueen AJ, Colaiácovo MP, McDonald K, Villeneuve AM (2002) Synapsis-dependent
654 and -independent mechanisms stabilize homolog pairing during meiotic prophase in C.
655 elegans. Genes Dev 16:2428–2442. doi: 10.1101/gad.1011602
656 16. Colaiácovo MP, MacQueen AJ, Martinez-Perez E, et al (2003) Synaptonemal complex
657 assembly in C. elegans is dispensable for loading strand-exchange proteins but critical for
658 proper completion of recombination. Dev Cell 5:463–474. doi: 10.1016/S1534-
659 5807(03)00232-6
660 17. Smolikov S, Eizinger A, Schild-Prüfert K, et al (2007) SYP-3 restricts synaptonemal
661 complex assembly to bridge paired chromosome axes during meiosis in Caenorhabditis
662 elegans. Genetics 176:2015–2025. doi: 10.1534/genetics.107.072413
663 18. Smolikov S, Schild-Prüfert K, Colaiácovo MP (2009) A yeast two-hybrid screen for SYP-3
664 interactors identifies SYP-4, a component required for synaptonemal complex assembly and
665 chiasma formation in Caenorhabditis elegans meiosis. PLoS Genet 5:e1000669. doi:
666 10.1371/journal.pgen.1000669
667 19. Schild-Prüfert K, Saito TT, Smolikov S, et al (2011) Organization of the synaptonemal
668 complex during meiosis in Caenorhabditis elegans. Genetics 189:411–421. doi:
669 10.1534/genetics.111.132431
670 20. Schücker K, Holm T, Franke C, et al (2015) Elucidation of synaptonemal complex
671 organization by super-resolution imaging with isotropic resolution. Proc Natl Acad Sci
672 112:2029–2033. doi: 10.1073/pnas.1414814112
673 21. Cahoon CK, Yu Z, Wang Y, et al (2017) Superresolution expansion microscopy reveals the
674 three-dimensional organization of theDrosophilasynaptonemal complex. Proc Natl Acad Sci
675 114:E6857–E6866. doi: 10.1073/pnas.1705623114
676 22. Rust MJ, Bates M, Zhuang X (2006) Sub-diffraction-limit imaging by stochastic optical
677 reconstruction microscopy (STORM). Nat Meth 3:793–795. doi: 10.1038/nmeth929
678 23. Huang B, Wang W, Bates M, Zhuang X (2008) Three-dimensional super-resolution imaging
679 by stochastic optical reconstruction microscopy. Science 319:810–813. doi:
680 10.1126/science.1153529

681 24. Köhler S, Wojcik M, Xu K, Dernburg AF (2017) Superresolution microscopy reveals the
682 three-dimensional organization of meiotic chromosome axes in intact Caenorhabditis elegans
683 tissue. Proc Natl Acad Sci 114:E4734–E4743. doi: 10.1073/pnas.1702312114
684 25. Zetka MC, Kawasaki I, Strome S, Müller F (1999) Synapsis and chiasma formation in
685 Caenorhabditis elegans require HIM-3, a meiotic chromosome core component that functions
686 in chromosome segregation. Genes Dev 13:2258–2270.
687 26. Gao J, Barroso C, Zhang P, et al (2016) N-terminal acetylation promotes synaptonemal
688 complex assembly in C. elegans. Genes Dev 30:2404–2416. doi: 10.1101/gad.277350.116
689 27. Schmekel K, Meuwissen RL, Dietrich AJ, et al (1996) Organization of SCP1 protein
690 molecules within synaptonemal complexes of the rat. Exp Cell Res 226:20–30. doi:
691 10.1006/excr.1996.0198
692 28. Sym M, Roeder GS (1995) Zip1-induced changes in synaptonemal complex structure and
693 polycomplex assembly. J Cell Biol 128:455–466.
694 29. Higgins JD, Sanchez-Moran E, Armstrong SJ, et al (2005) The Arabidopsis synaptonemal
695 complex protein ZYP1 is required for chromosome synapsis and normal fidelity of crossing
696 over. Genes Dev 19:2488–2500. doi: 10.1101/gad.354705
697 30. Meuwissen RL, Offenberg HH, Dietrich AJ, et al (1992) A coiled-coil related protein
698 specific for synapsed regions of meiotic prophase chromosomes. EMBO J 11:5091–5100.
699 31. Anderson LK, Royer SM, Page SL, et al (2005) Juxtaposition of C(2)M and the transverse
700 filament protein C(3)G within the central region of Drosophila synaptonemal complex. Proc
701 Natl Acad Sci USA 102:4482–4487. doi: 10.1073/pnas.0500172102
702 32. Rog O, Dernburg AF (2015) Direct Visualization Reveals Kinetics of Meiotic Chromosome
703 Synapsis. Cell Rep 10:1639–1645. doi: 10.1016/j.celrep.2015.02.032
704 33. Reynolds A, Qiao H, Yang Y, et al (2013) RNF212 is a dosage-sensitive regulator of
705 crossing-over during mammalian meiosis. Nat Genet 45:269–278. doi: 10.1038/ng.2541
706 34. Qiao H, Prasada Rao HBD, Yang Y, et al (2014) Antagonistic roles of ubiquitin ligase HEI10
707 and SUMO ligase RNF212 regulate meiotic recombination. Nat Genet 46:194–199. doi:
708 10.1038/ng.2858
709 35. de Gennes PG, Prost J (1993) The Physics of Liquid Crystals, 2nd ed. Clarendon Press,
710 Oxford

711 36. Yokoo R, Zawadzki KA, Nabeshima K, et al (2012) COSA-1 reveals robust homeostasis and
712 separable licensing and reinforcement steps governing meiotic crossovers. Cell 149:75–87.
713 doi: 10.1016/j.cell.2012.01.052
714 37. Harper NC, Rillo R, Jover-Gil S, et al (2011) Pairing centers recruit a Polo-like kinase to
715 orchestrate meiotic chromosome dynamics in C. elegans. Dev Cell 21:934–947. doi:
716 10.1016/j.devcel.2011.09.001
717 38. Sato-Carlton A, Nakamura-Tabuchi C, Chartrand SK, et al (2018) Phosphorylation of the
718 synaptonemal complex protein SYP-1 promotes meiotic chromosome segregation. The
719 Journal of Cell Biology 217:555–570. doi: 10.1083/jcb.201707161
720 39. Jantsch V, Pasierbek P, Mueller MM, et al (2004) Targeted gene knockout reveals a role in
721 meiotic recombination for ZHP-3, a Zip3-related protein in Caenorhabditis elegans. Mol Cell
722 Biol 24:7998–8006. doi: 10.1128/MCB.24.18.7998-8006.2004
723 40. Labella S, Woglar A, Jantsch V, Zetka M (2011) Polo kinases establish links between
724 meiotic chromosomes and cytoskeletal forces essential for homolog pairing. Dev Cell
725 21:948–958. doi: 10.1016/j.devcel.2011.07.011
726 41. Kim Y, Kostow N, Demburg AF (2015) The Chromosome Axis Mediates Feedback Control
727 of CHK-2 to Ensure Crossover Formation in C. elegans. Dev Cell 35:247–261. doi:
728 10.1016/j.devcel.2015.09.021
729 42. Hillers KJ, Villeneuve AM (2003) Chromosome-wide control of meiotic crossing over in C.
730 elegans. Curr Biol 13:1641–1647. doi: 10.1038/nrg1210
731 43. Nabeshima K, Villeneuve AM, Colaiácovo MP (2005) Crossing over is coupled to late
732 meiotic prophase bivalent differentiation through asymmetric disassembly of the SC. J Cell
733 Biol 168:683–689. doi: 10.1083/jcb.200410144
734 44. Broman KW, Weber JL (2000) Characterization of human crossover interference. Am J Hum
735 Genet 66:1911–1926. doi: 10.1086/302923
736 45. Muller HJ (1916) The mechanism of crossing-over IV. American Naturalist 50:421–434.
737 46. Drouaud J, Mercier R, Chelysheva L, et al (2007) Sex-specific crossover distributions and
738 variations in interference level along Arabidopsis thaliana chromosome 4. PLoS Genet
739 3:e106. doi: 10.1371/journal.pgen.0030106

740 47. Petkov PM, Broman KW, Szatkiewicz JP, Paigen K (2007) Crossover interference underlies
741 sex differences in recombination rates. Trends Genet 23:539–542. doi:
742 10.1016/j.tig.2007.08.015
743 48. Mets DG, Meyer BJ (2009) Condensins Regulate Meiotic DNA Break Distribution, thus
744 Crossover Frequency, by Controlling Chromosome Structure. Cell 139:73–86. doi:
745 10.1016/j.cell.2009.07.035
746 49. Zhang L, Liang Z, Hutchinson J, Kleckner N (2014) Crossover Patterning by the Beam-Film
747 Model: Analysis and Implications. PLoS Genet 10:e1004042. doi:
748 10.1371/journal.pgen.1004042
749 50. Goodyer W, Kaitna S, Couteau F, et al (2008) HTP-3 links DSB formation with homolog
750 pairing and crossing over during C. elegans meiosis. Dev Cell 14:263–274. doi:
751 10.1016/j.devcel.2007.11.016
752 51. Kleckner N, Zickler D, Jones GH, et al (2004) A mechanical basis for chromosome function.
753 Proc Natl Acad Sci USA 101:12592–12597. doi: 10.1073/pnas.0402724101
754 52. Brenner S (1974) The genetics of Caenorhabditis elegans. Genetics 77:71–94.
755 53. Frøkjær-Jensen C, Davis MW, Hopkins CE, et al (2008) Single-copy insertion of transgenes
756 in Caenorhabditis elegans. Nat Genet 40:1375–1383. doi: 10.1038/ng.248
757 54. Dickinson DJ, Ward JD, Reiner DJ, Goldstein B (2013) Engineering the Caenorhabditis
758 elegans genome using Cas9-triggered homologous recombination. Nat Meth 10:1028–1034.
759 doi: 10.1038/nmeth.2641
760 55. Redemann S, Schloissnig S, Ernst S, et al (2011) Codon adaptation-based control of protein
761 expression in C. elegans. Nat Meth 8:250–252. doi: 10.1038/nmeth.1565
762 56. Phillips CM, McDonald KL, Dernburg AF (2009) Cytological analysis of meiosis in
763 Caenorhabditis elegans. Methods Mol Biol 558:171–195. doi: 10.1007/978-1-60761-103-
764 5_11
765 57. Macqueen AJ, Phillips CM, Bhalla N, et al (2005) Chromosome sites play dual roles to
766 establish homologous synapsis during meiosis in C-elegans. Cell 123:1037–1050. doi:
767 10.1016/j.cell.2005.09.034
768 58. Gerstein MB, Lu ZJ, Van Nostrand EL, et al (2010) Integrative analysis of the
769 Caenorhabditis elegans genome by the modENCODE project. Science 330:1775–1787. doi:
770 10.1126/science.1196914

771 59. McKinney SA, Murphy CS, Hazelwood KL, et al (2009) A bright and photostable
772 photoconvertible fluorescent protein for fusion tags. Nat Meth 6:131–133. doi:
773 10.1038/nmeth.1296
774 60. Wang S, Moffitt JR, Dempsey GT, et al (2014) Characterization and development of
775 photoactivatable fluorescent proteins for single-molecule-based superresolution imaging.
776 Proc Natl Acad Sci 111:8452–8457. doi: 10.1073/pnas.1406593111
777 61. Meyer M, Kircher M (2010) Illumina sequencing library preparation for highly multiplexed
778 target capture and sequencing. Cold Spring Harb Protoc 2010:pdb.prot5448. doi:
779 10.1101/pdb.prot5448
780 62. Thompson OA, Snoek LB, Nijveen H, et al (2015) Remarkably Divergent Regions Punctuate
781 the Genome Assembly of the Caenorhabditis elegans Hawaiian Strain CB4856. Genetics
782 200:975–989. doi: 10.1534/genetics.115.175950
783 63. Andolfatto P, Davison D, Erezyilmaz D, et al (2011) Multiplexed shotgun genotyping for
784 rapid and efficient genetic mapping. Genome Res 21:610–617. doi: 10.1101/gr.115402.110
785 64. McDonald KL, Webb RI (2011) Freeze substitution in 3 hours or less. J Microsc 243:227–
786 233. doi: 10.1111/j.1365-2818.2011.03526.x
787 65. McDonald KL (2014) Rapid embedding methods into epoxy and LR White resins for
788 morphological and immunological analysis of cryofixed biological specimens. Microsc
789 Microanal 20:152–163. doi: 10.1017/S1431927613013846
790
791